Chemical Science

ROYAL SOCIETY OF CHEMISTRY

EDGE ARTICLE

View Article Online
View Journal | View Issue

Cite this: *Chem. Sci.*, 2022, **13**, 5693

All publication charges for this article have been paid for by the Royal Society of Chemistry

Received 27th January 2022
Accepted 1st April 2022

DOI: 10.1039/d2sc00526c

rsc.li/chemical-science

Designable assembly of atomically precise Al_4O_4 cubane supported mesoporous heterometallic architectures†

Ya-Jie Liu,[ab] Yinghua Yu,[a] Yi-Fan Sun,[a] Wei-Hui Fang *[a] and Jian Zhang *[a]

Heterometallic cluster-based framework materials are of interest in terms of both their porous structures and multi-metallic reactivity. However, such materials have not yet been extensively investigated because of difficulties in their synthesis and structural characterization. Herein, we reported the designable synthesis of atomically precise heterometallic cluster-based framework compounds and their application as catalysts in aldol reactions. By using the synergistic coordination protocol, we successfully isolated a broad range of compounds with the general formula, $[Al_4M_4O_4(L)_{12}(DABCO)_2]$ (L = carboxylates; DABCO = 1,4-diazabicyclo[2.2.2]-octane; M^{2+} = Co^{2+}, Mn^{2+}, Zn^{2+}, Fe^{2+}, Cd^{2+}). The basic heterometallic building blocks contain unprecedented main-group γ-alumina moieties and surrounding unsaturated transition metal centers. Interestingly, the porosity and interpenetration of these frameworks can be rationally regulated through the unprecedented strategy of increment of the metal radius in addition to general introduction of sterically bulky groups on the ligand. Furthermore, these porous materials are effective catalysts for aldol reactions. This work provides a catalytic molecular model platform with accurate molecular bonding between the supporters and catalytically active metal ions.

Introduction

Aluminosilicate zeolites with 4-connected metal centers are a class of inorganic porous solids with a range of applications in catalysis, ion exchange and separation.[1–6] Compared with these traditional 4-connected nodes,[7–18] the use of polynuclear metal clusters as 4-connected nodes is highly desirable because of the availability of large pore sizes and the possibility of combining unique cluster-based properties.[19–22] Such an idea has been realized by Feng *et al.*[22,23] *via* the assembly of supertetrahedral metal–chalcogenide clusters. Most significantly, elements without tetrahedral geometry can be incorporated, thus providing access to multifunctional framework materials with zeolite type topology.[24–26]

Heterometallic oxo clusters may exhibit unique properties resulting from the synergy effect of the two substantially different types of metal ions. Therefore, it is of great interest to incorporate heterometallic clusters as 4-connected centers. However, extensive studies based on 4-connected heterometallic clusters remain scarce because of the lack of a strategy for efficient synthesis. There are two possible synthetic challenges: (1) competitive coordination and integration of two kinds of metal ions, and (2) metal clusters with high nuclearity and positive charge are prone to accepting more organic ligands, thus leading to highly-connected dense topologies. Once the building blocks are established, effective interpenetration regulation is another issue that should be considered.[27,28] In 2019, Zheng *et al.*[29] summarized advances in the design and synthesis of cluster organic frameworks based on 4-connected metal–halide clusters,[30] metal–oxygen clusters,[31] and metal–chalcogen clusters.[32] In the domain of metal–oxygen clusters, only transition metal clusters (such as ε-Zn_4PMo_{12} [26] or Cd_4Cu_6 [33]) have been reported as 4-connected nodes. However, main group element-based examples are challenging and still lacking.

γ-Al_2O_3 is one of the most common kinds of alumina, which has a large surface area, and strong adsorption capacity and has been widely used in adsorbents, catalysts and catalyst supports.[34] With our recent research in Al(III) chemistry, we herein demonstrate a synergistic coordination strategy towards the assembly of 4-connected heterometallic cluster-based framework materials. The strategy is based on spontaneous selective coordination between two kinds of metal centers (Al centers and d-transition metals) and two types of ligands (chelating L with O-donors and bridging DABCO with N donors,

[a]*State Key Laboratory of Structural Chemistry, Fujian Institute of Research on the Structure of Matter, Chinese Academy of Sciences, 350002 Fuzhou, P. R. China. E-mail: fwh@fjirsm.ac.cn; zhj@fjirsm.ac.cn*

[b]*University of Chinese Academy of Sciences, Beijing 100049, P. R. China*

† Electronic supplementary information (ESI) available: Experimental section, detailed structure charts, stability analysis, sorption isotherms, characterization, catalytic mechanism, and tables. The structures reported in this article have been deposited at the Cambridge Crystallographic Data Centre (CCDC). CCDC 2056099–2056118, 2056127, 2156657 (**AlOC-99–AlOC-120**). For ESI and crystallographic data in CIF or other electronic format see **https://doi.org/10.1039/d2sc00526c**

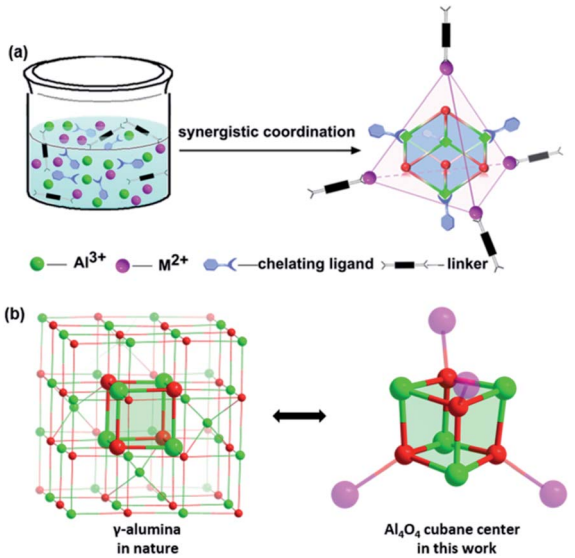

Scheme 1 (a) Scheme demonstrating the synergistic coordination synthetic strategy; (b) comparison between the structures of γ-Al_2O_3 and the Al_4O_4 cubane in a tetrahedral cluster node.

respectively) (Scheme 1a).[35] Such an approach is universal and we successfully isolate a broad range of compounds [Al_4O_4-$M_4(L)_{12}(DABCO)_2$] (denoted as AlOCs; M^{2+} = Mn^{2+}, Fe^{2+}, Co^{2+}, Zn^{2+}, Cd^{2+}, L = carboxylates; DABCO = 1,4-diazabicyclo[2.2.2] octane) (Table 1). We were surprised to find that the Al_4O_4 cubane (denoted as the γ-alumina moiety) is located in the center of the 4-connected nodes (Scheme 1b).[36,37] In addition, both the inorganic and organic shells of the Al_4O_4 cubane can be modified to a large extent. Interestingly, controllable interpenetration is realized through the introduction of sterically bulky groups, increment of the ionic radius of transition metal ions, and variation of the M^{2+}/Al^{3+} concentration. Furthermore, these porous materials are effective catalysts for aldol reactions.

Table 1 A summary of the 4-connected AlOCs[a]

Complex	Composition	Sp. Gr.	R_1 Value	Void ratio
Two-fold diamond (*dia*) interpenetration				
AlOC-99	$Al_4Co_4O_4(BA)_{12}(DABCO)_2$	$Fd\bar{3}c$	0.0801	1.2%
AlOC-100	$Al_4Co_4O_4(2\text{-}FBA)_{12}(DABCO)_2$	$Fd\bar{3}c$	0.0759	No
AlOC-101	$Al_4Co_4O_4(3\text{-}FBA)_{12}(DABCO)_2$	$Fd\bar{3}c$	0.1149	7.6%
AlOC-102	$Al_4Co_4O_4(4\text{-}FBA)_{12}(DABCO)_2$	$Fd\bar{3}c$	0.1474	2.5%
AlOC-103	$Al_4Co_4O_4(2\text{-}FA)_{12}(DABCO)_2$	$Fd\bar{3}c$	0.0998	2.8%
AlOC-104	$Al_4Co_4O_4(2\text{-}TA)_{12}(DABCO)_2$	$Fd\bar{3}c$	0.1447	1.6%
AlOC-105	$Al_4Co_4O_4(3\text{-}TA)_{12}(DABCO)_2$	$Fd\bar{3}c$	0.1274	2.4%
AlOC-106	$Al_4Mn_4O_4(BA)_{12}(DABCO)_2$	$Fd\bar{3}c$	0.0858	No
AlOC-107	$Al_4Fe_4O_4(BA)_{12}(DABCO)_2$	$Fd\bar{3}c$	0.0566	1.0%
AlOC-108	$Al_4Zn_4O_4(BA)_{12}(DABCO)_2$	$Fd\bar{3}c$	0.0548	1.0%
Non-interpenetrated diamond (*dia*) topology				
AlOC-109	$Al_4Co_4O_4(3\text{-}MBA)_{12}(DABCO)_2$	$F4_132$	0.0736	42.5%
AlOC-110	$Al_4Fe_4O_4(BA)_{12}(DABCO)_2$	$F4_132$	0.0634	52.8%
AlOC-111	$Al_4Cd_4O_4(BA)_{12}(DABCO)_2$	$F4_132$	0.0751	55.6%
Non-interpenetrated lonsdaleite (*lon*) topology				
AlOC-112	$Al_4Co_4O_4(BA)_{12}(DABCO)_2$	$P\bar{6}2c$	0.0629	53.9%
AlOC-113	$Al_4Co_4O_4(3\text{-}FBA)_{12}(DABCO)_2$	$P\bar{6}2c$	0.0809	47.0%
AlOC-114	$Al_4Co_4O_4(4\text{-}CBA)_{12}(DABCO)_2$	$P\bar{6}2c$	0.0757	44.9%
AlOC-115	$Al_4Co_4O_4(4\text{-}MBA)_{12}(DABCO)_2$	$P\bar{6}2c$	0.0736	44.3%
AlOC-116	$Al_4Co_4O_4(4\text{-}ABA)_{12}(DABCO)_2$	$P\bar{6}2c$	0.0972	48.4%
AlOC-117	$Al_4Mn_4O_4(BA)_{12}(DABCO)_2$	$P\bar{6}2c$	0.0576	54.3%
AlOC-118	$Al_4Fe_4O_4(BA)_{12}(DABCO)_2$	$P\bar{6}2c$	0.1081	53.3%
AlOC-119	$Al_4Zn_4O_4(BA)_{12}(DABCO)_2$	$P\bar{6}2c$	0.0542	53.5%
AlOC-120	$Al_4Cd_4O_4(BA)_{12}(DABCO)_2$	$P\bar{6}2c$	0.0784	56.4%

[a] Abbreviations: BA = benzoate; 2-FBA = 2-fluorobenzoate; 3-FBA = 3-fluorobenzoate; 4-FBA = 4-fluorobenzoate; 2-FA = 2-furan formate; 2-TA = 2-thiophene formate; 3-TA = 3-thiophene formate; 3-MBA = 3-methylbenzoate; 4-MBA = 4-methylbenzoate; 4-CBA = 4-chlorobenzoate; 4-ABA = 4-aminobenzoate.

Experimental

Materials and general methods

All the reagents and solvents employed were commercially available and used without further purification. $Al(O^iPr)_3$ was acquired from Aladdin Chemical Reagent Shanghai. $Fe(Ac)_2$ was obtained from TCI. Acetonitrile (99%), benzoic acid, $Co(Ac)_2 \cdot 4H_2O$, $MnCl_2 \cdot 4H_2O$, $Zn(Ac)_2 \cdot 2H_2O$ and $Cd(Ac)_2 \cdot 2H_2O$ were bought from Sinopharm Chemical Reagent Beijing. $Ti(O^iPr)_4$ and other carboxylic acids were purchased from Adamas-beta.

The energy dispersive spectroscopy (EDS) analyses of single crystals were performed on a JEOL JSM6700F field-emission scanning electron microscope equipped with an Oxford INCA system. IR spectra (KBr pellets) were recorded on an ABB Bomem MB102 spectrometer over a range of 400–3900 cm^{-1}. Powder X-ray diffraction (PXRD) data were collected on a Rigaku Mini Flex II diffractometer using CuKα radiation (λ = 1.54056 Å) under ambient conditions. The UV-vis diffuse reflection data were recorded at room temperature using a powder sample with $BaSO_4$ as a standard (100% reflectance) on a PerkinElmer Lamda-950 UV spectrophotometer and scanned at 200–1200 nm. The absorption data were calculated from the Kubelka–Munk function, $(F(R) = (1 - R)^2/2R)$, where R represents the reflectance.[38] Surface chemical analyses were performed by X-ray photoelectron spectroscopy (XPS, Thermo Fisher, ESCALAB 250Xi). Metal proportional analyses were performed on an Ultima-2 inductively coupled plasma (ICP) spectrometer. The TGA curves were recorded in the region of 30–800 °C at a heating rate of 10 °C min^{-1} in a flowing N_2 atmosphere on a Mettler Toledo TGA/SDTA 851^e analyzer.

Synthesis of two-fold interpenetrated diamond (*dia*) frameworks AlOC-99–AlOC-108

$Al(O^iPr)_3$ (0.918 g, 4.5 mmol), $Co(Ac)_2 \cdot 4H_2O$ (0.75–2.5 g, 3–10 mmol), DABCO (0.224 g, 1 mmol) and benzoic acid (0.978 g, 8 mmol) were dissolved in acetonitrile (10 mL), and then $Ti(O^iPr)_4$ (0.5 mL, 1.5 mmol) was added to the bottle and mixed at room temperature. The resultant solution was sealed in a Teflon-lined autoclave (23 mL) and heated at 160 °C for three days. After being cooled to room temperature, red octahedral crystals of **AlOC-99** were obtained (maximum yield: ~64% (1.5 g) for **AlOC-99** based on $Al(O^iPr)_3$. Synthesis of **AlOC-100–AlOC-105** is similar to that of **AlOC-99** except that benzoic acid was replaced by 2-FBA, 3-FBA, 4-FBA, 2-FA, 2-TA, and 3-TA. Red octahedral

crystals were collected after about three days (maximum yield: ~10% (260 mg), ~7% (180 mg), ~11% (290 mg), ~1.5% (30 mg), ~1.6% (40 mg), and ~1.2% (30 mg) based on $Al(O^iPr)_3$ for **AlOC-100–AlOC-105**, respectively). Synthesis of **AlOC-106–AlOC-108** is similar to that of **AlOC-99** except that $Co(Ac)_2\cdot 4H_2O$ was replaced by $MnCl_2\cdot 4H_2O$, $Fe(Ac)_2$ and $Cd(Ac)_2\cdot 2H_2O$. Yellow or colorless octahedral crystals were collected after about three days (maximum yield: ~19% (450 mg), ~1.9% (50 mg), and ~4.6% (110 mg) for **AlOC-106–AlOC-108**.

Synthesis of non-interpenetrated diamond (*dia*) frameworks AlOC-109–AlOC-111

Synthesis of **AlOC-109–AlOC-111** is similar to that of **AlOC-99** except that benzoic acid was replaced by 3-methylbenzoic acid or $Co(Ac)_2\cdot 4H_2O$ was replaced by $Fe(Ac)_2$ and $Cd(Ac)_2\cdot 2H_2O$. Red (**AlOC-109**), yellow (**AlOC-110**) or colorless (**AlOC-111**) octahedral crystals were collected after about three days (maximum yield: ~20.5% (520 mg), ~3.4% (80 mg) and ~1.16% (30 mg) for **AlOC-109–AlOC-111** based on $Al(O^iPr)_3$).

Synthesis of non-interpenetrated lonsdaleite (*lon*) frameworks AlOC-112–AlOC-120

The synthetic procedure of **AlOC-112** is similar to that of **AlOC-99**, except that the amount of $Co(Ac)_2\cdot 4H_2O$ was reduced to 1–2 mmol. Finally, red hexagonal flaky crystals of **AlOC-112** were obtained (maximum yield: ~34% (800 mg) for **AlOC-112** based on $Al(O^iPr)_3$). Synthesis of **AlOC-113–AlOC-116** is similar to that of **AlOC-112** except that benzoic acid was replaced by 3-FBA, 4-CBA, 4-MBA and 4-ABA. Red hexagonal flaky crystals were collected after about three days (maximum yield: ~23% (600 mg), ~18% (500 mg), ~32% (800 mg), and ~8.2% (210 mg) for **AlOC-113–AlOC-116** based on $Al(O^iPr)_3$). Synthesis of **AlOC-117–AlOC-120** is similar to that of **AlOC-112** except that $Co(Ac)_2\cdot 4H_2O$ was replaced by $MnCl_2\cdot 4H_2O$, $Fe(Ac)_2$, $Zn(Ac)_2\cdot 2H_2O$ and $Cd(Ac)_2\cdot 2H_2O$. Yellow or colorless hexagonal flaky crystals were collected after about three days (maximum yield: ~51.5% (1.2 g), ~1.7% (40 mg), ~12.6% (300 mg) and ~2.2% (60 mg) for **AlOC-117–AlOC-120** based on $Al(O^iPr)_3$).

Caution: The synthesis of **AlOC-107** should be performed in a glovebox in a vacuum environment and nitrogen should be pumped into the reactor for removing the soluble oxygen from the solvent. Yellow crystals of freshly prepared Fe-containing compounds (**AlOC-107**, **AlOC-110** and **AlOC-118**) can gradually turn red due to the rapid oxidation when exposed to air.

General methods for X-ray crystallography

Crystallographic data of **AlOC-106** and **AlOC-119** were collected on a Mercury single crystal diffractometer equipped with graphite-monochromatic Mo Kα radiation (λ = 0.71073 Å). Compounds **AlOC-117** and **AlOC-118** were collected on a Supernova single crystal diffractometer equipped with graphite-monochromated Cu Kα radiation (λ = 1.54184 Å). Other compounds (**AlOC-99–AlOC-105**, **AlOC-107–AlOC-116**, and **AlOC-120**) were collected on a Hybrid Pixel Array detector equipped with graphite-monochromated Ga Kα radiation (λ = 1.3405 Å). The structures were solved with direct methods using OLEX[2] and refined by full-matrix least-squares on F^2 using SHELXTL.[39] Contributions to scattering due to disordered solvent molecules were removed using the SQUEEZE routine of PLATON. All hydrogen atoms were theoretically positioned, riding on the concerned atoms and refined with fixed thermal factors. Non-hydrogen atoms were refined anisotropically.

Preparation of active samples for gas adsorption

Crystals were soaked in ethanol and heated at 80 °C for one week. During this time, the ethanol solution should be exchanged several times a day. Subsequently, the sample was degassed under a dynamic vacuum at 100 °C for 6 h to activate the sample. The gas adsorption isotherms of active samples were obtained on a Micromeritics ASAP 2020 volumetric adsorption instrument.

Results and discussion

The tunable shell of Al_4O_4 supported supertetrahedral nodes

The prominent feature of these compounds is the presence of a central Al_4O_4 γ-alumina moiety. The accurate crystal structures of Al_4N_4,[40] Al_4P_4, Al_4S_4 [41] and Al_4Se_4 [42] have been reported, while the Al_4O_4 cubane has never been reported and has only been studied computationally.[43] However, the Al_4O_4 cubane can act as a subunit that exists in high-nuclearity AlOCs (Al_{30}, Cu_2Al_{30}-S, and Zn_2Al_{32}).[44–46] In this work, the Al_4O_4 cubane serves as a cornerstone in supertetrahedron nodes, where both inorganic (M^{2+} = Co, Mn, Zn, Fe, Cd) and organic (a broad range of chelated aromatic carboxylates) compositions are tunable (Fig. 1). And as many as 22 isostructural compounds were

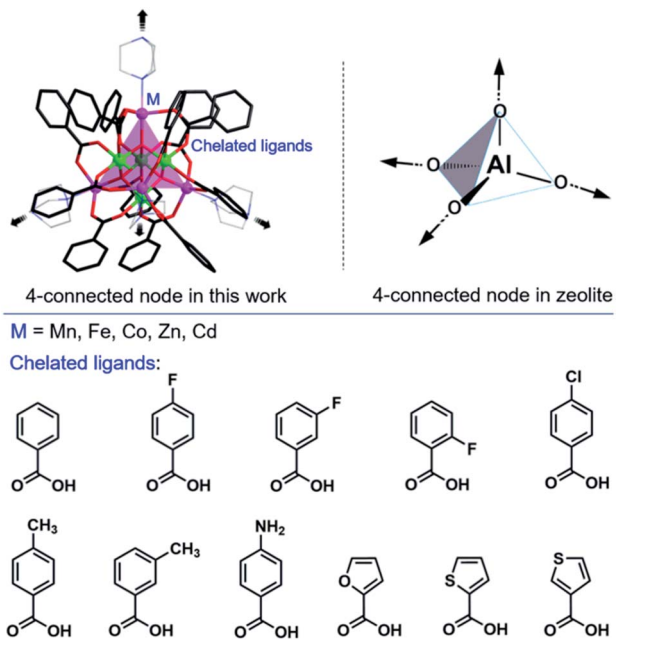

Fig. 1 The tunable inorganic metal ion shell and organic chelated ligand shell on tetrahedral cluster nodes. The atom color code: O, red; C, dark grey and black; N, blue; Al, green. Hydrogen atoms are omitted for clarity.

successfully isolated (Table 1, **AlOC-99–AlOC-120**, Fig. S1–S22†). Each Al atom in all compounds adopts a six-coordination geometry, bonding to three μ_4-O atoms and three carboxylate oxygen atoms (O_{COO}) (Fig. S23†). Every external M ion resided in a trigonal bipyramid environment with three O_{COO} atoms, one μ_4-O bridge and one N atom from DABCO. Each triangular face of the supertetrahedral core is consolidated by three bridging bidentate chelating ligands (Fig. S24 and S25†). Compared with the charged tetrahedral cages,[47–49] the supertetrahedral cluster $[Al_4Co_4O_4(L)_{12}]$ herein is neutral. Four DABCO linkers on the cluster node allow further connections, which is similar to the 4-connected TO_4 (T = Si, Al, P, *etc.*) node in inorganic zeolite materials.

Interpenetration regulation

As shown in Fig. 2, the 4-connected frameworks are categorized into three types. $[Al_4M_4O_4(L)_{12}(DABCO)_2]$ undergoes a change in the degree of interpenetration from a dense doubly interpenetrated framework (**AlOC-99–AlOC-108**, Fig. S1–S10†) to two kinds of highly porous non-interpenetrated framework with diamond (*dia*) topology: **AlOC-109–AlOC-111**, Fig. S11–S13;† and lonsdaleite (*lon*) topology (**AlOC-112–AlOC-120**, Fig. S14–S22†). It is reported that factors that affect interpenetration include pressure, temperature, solvent, ligand design, *etc.*[27,50,51] Herein, precise suppression of interpenetration by an increment of the metal radius is found in addition to the ligand design and concentration ratio of M^{2+}/Al^{3+}.

Interpenetration regulation through ligand design. The regulation of the topology is greatly related to the types of ligands. For benzoate or fluorobenzoate, both interpenetrated and non-interpenetrated frameworks can be obtained (interpenetrated diamond (*dia*) topology: **AlOC-99–AlOC-102**; non-interpenetrated lonsdaleite (*lon*) topology: **AlOC-112** and **AlOC-113**). However, if large steric groups (–Cl, $–CH_3$ and $–NH_2$) are introduced, only non-interpenetrated frameworks can be generated (**AlOC-109** and **AlOC-114–AlOC-116**) (Fig. 2c, d and S11, S16–S18†). Intriguingly, the presence of the substituents can also enhance the intermolecular and intramolecular hydrogen bond interactions (Fig. S26†). For smaller pentacyclic carboxylates, only doubly interpenetrated frameworks (**AlOC-103–AlOC-105**) were synthesized (Fig. S5–S7†).

Interpenetration regulation through increasing the ionic radius of TM ions. Cd-containing frameworks (**AlOC-111** and **AlOC-120**) present non-interpenetrated topologies (Fig. 2e, f and S13, S22†), which are different from those of Mn, Fe, Co, and Zn involving compounds. A possible reason is attributed to its larger radius, and the size of $Cd_4Al_4O_4$ tetrahedral clusters is obviously larger than that of other ones (Fig. S27†). Although a large number of factors influencing interpenetration have been reported, the effect of the ionic radius was discovered for the first time.

Interpenetration regulation through altering the ratio of M^{2+}/Al^{3+}. The variation of the mole ratio of raw materials has a great impact on the structural types.[8,50] Herein, the M^{2+}/Al^{3+} concentration plays an important role in interpenetration regulation. For example, when the ratio of Co^{2+}/Al^{3+} is greater than 1.11, the pure octahedral crystals with a doubly interpenetrated diamond (*dia*) framework can be obtained (Fig. 2a and b, **AlOC-99**, $Fd\bar{3}c$; Fig. 3a, left), in which the 6^6 diamond (*dia*) cage is exclusively made up of six chair-like six-membered rings (Fig. 3b, left). When the ratio of Co^{2+}/Al^{3+} is lower than 0.44, only pure hexagonal flaky crystals with non-interpenetrated lonsdaleite (*lon*) topologies can be generated (Fig. 2g, h and S14,† **AlOC-112**, $P\bar{6}2c$; Fig. 3a, right). Different from the 6^6 diamond (*dia*) cage, the 6^5 lonsdaleite (*lon*) cage in **AlOC-112** is composed of chair-like and boat-like six-membered rings

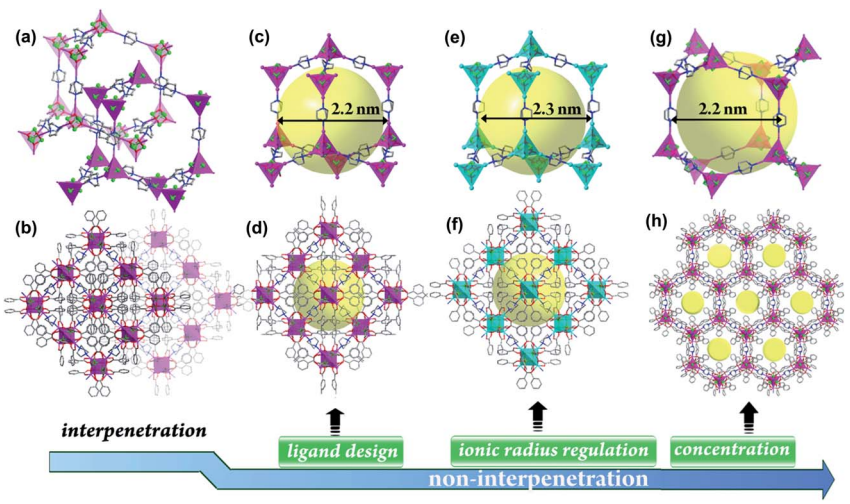

Fig. 2 The interpenetration regulation strategies: introduction of sterically bulky groups, increment of the ionic radius and decrease of the M^{2+}/Al^{3+} concentration. The mesoporous cavities (a, c, e, and g) and overall frameworks (b, d, f, and h) in two-fold interpenetrated **AlOC-99**, and non-interpenetrated **AlOC-109**, **AlOC-111** and **AlOC-112**, respectively. The atom color code: O, red; C, dark grey; N, blue; Co, pink; Cd, turquoise; Al, green. Hydrogen atoms are omitted for clarity. The diamond (*dia*) frameworks present rhombic windows, while the lonsdaleite (*lon*) frameworks possess hexagonal channels (diameter: 3.761 nm; interior wall diameter: 0.909 nm) aligned parallel to the *c*-axis.

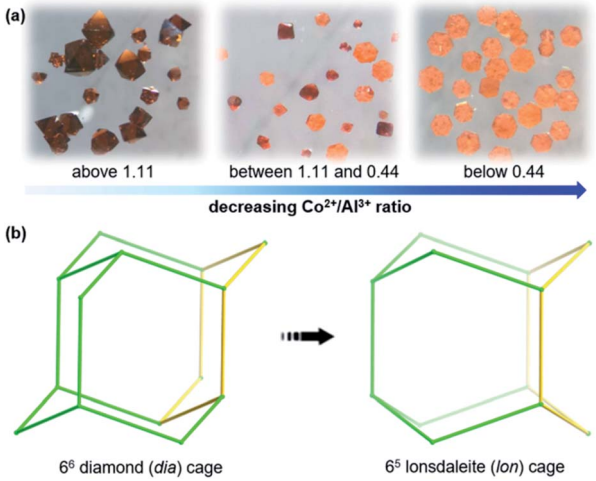

Fig. 3 (a) Photos of reaction products obtained from controlling the ratio of Co^{2+}/Al^{3+}. (b) The simplified diamond (*dia*) and lonsdaleite (*lon*) cages. Chair-like (left) and boat-like (right) six-membered rings have been highlighted with yellow bonds.

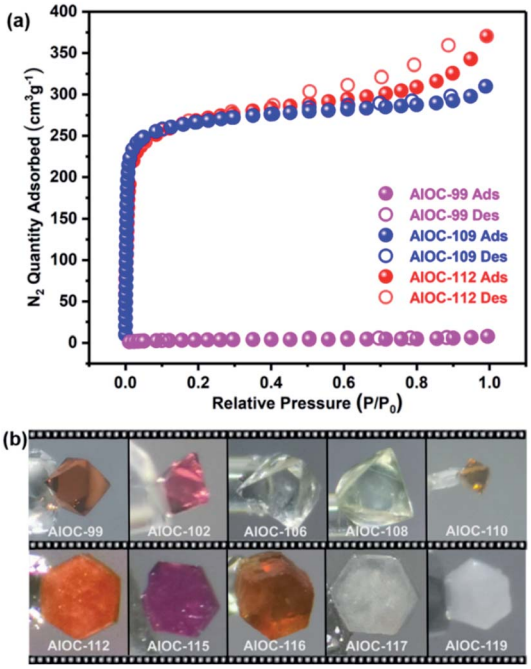

Fig. 4 (a) The N_2 sorption isotherms of **AlOC-99**, **AlOC-109** and **AlOC-112**. (b) Crystal photos of representative samples.

(Fig. 3b, right). However, when the ratio of Co^{2+}/Al^{3+} is controlled between 0.44 and 1.11, the product was a mixture phase containing both octahedral crystals and hexagonal flaky crystals (Fig. 3a, middle).

Therefore, it is reasonable to infer that the low M^{2+}/Al^{3+} ratio favored the non-interpenetrated lonsdaleite (*lon*) form,[52] which is supported by the experimental results that come from the isolation of a series of isostructural Mn, Fe, Zn and Cd constructed AlOCs (**AlOC-117–AlOC-120**; Table 1, Fig. S19–S22†). For Fe constructed frameworks, the control of the Fe^{2+}/Al^{3+} ratio is not easy due to the rapid oxidation of Fe^{2+}. Thus, the synthesis of the doubly interpenetrated diamond (*dia*) framework of **AlOC-107** with a high Fe^{2+}/Al^{3+} ratio should be performed in a glovebox under pumped nitrogen. Instead, non-interpenetrated *dia* framework **AlOC-110** will be generated when synthesized under the same conditions without nitrogen.

Physical performance

The non-interpenetrated framework density (for example, **AlOC-112** (0.823 g cm^{-3})) is approximately half that of doubly interpenetrated **AlOC-99** (1.651 g cm^{-3}). The formation of a non-interpenetrated framework is noteworthy given the mesoporous cavity channels (*ca.* 2.2–2.3 nm) (Fig. 2c, e, g and S30†). Correspondingly, it also exhibits obvious higher solvent-accessible volumes (*e.g.*, 53.9% for **AlOC-112** calculated using PLATON).[53] Considering their potential application in gas adsorption and separation, N_2 sorption tests were conducted to evaluate porosity. Based on N_2 sorption isotherms, the BET surface areas were calculated to be 11.48, 779.6 and 797.2 $m^2\ g^{-1}$ for **AlOC-99**, **AlOC-109** and **AlOC-112** (Fig. 4a and S31†). The pronounced H4 hysteresis loops of **AlOC-109** and **AlOC-112** are located at high P/P_0 (P/P_0 = 0.4–1.0), further confirming the presence of the mesopores in the materials.[54,55] The experimental CO_2 uptake of **AlOC-99**, **AlOC-109** and **AlOC-112** was measured to be 10.2, 13.9 and 21.7 $cm^3\ g^{-1}$ at 273 K.

The stability of frameworks plays an important role in research and industrial production, because it provides an applicable scope of the material. Their stability is related to interpenetration and topology. For example, the doubly interpenetrated framework is thermodynamically stable when heated to 300 °C, while the non-interpenetrated ones can only tolerate 250 °C (Fig. S32 and S33†), indicating that interpenetration in **AlOC-99** obviously enhances the stability of the framework. In addition, **AlOC-99** and **AlOC-109** were stable after being immersed in an aqueous solution with different pH values (Fig. S34 and S35†). The lonsdaleite (*lon*) framework of **AlOC-112** will collapse gradually in water, indicating that the diamond (*dia*) type framework is more stable than that of lonsdaleite (*lon*). Nevertheless, both of them were stable in common organic solvents, including MeOH, EtOH, MeCN, DMF and DMSO (Fig. S36†). Their solution stabilities are related to hydrophobic wettability. And the measured contact angles for **AlOC-99**, **AlOC-109** and **AlOC-112** are 160.58°, 140.13° and 153.23°, respectively (Fig. S37 and S38†).[56] Furthermore, all three materials can remain in the air for more than one year (Fig. S39†), which is related to the presence of the Al_4O_4 core because compounds like Co_2Bdc_2Dabco without aluminium (Fig. S40†) cannot be exposed to air for more than two weeks.[57,58]

These compounds were all characterized by powder X-ray diffraction (PXRD), IR spectroscopy, and energy dispersive spectroscopy (EDS) analyses (Fig. S41–S68†). The atomic ratio of M to Al was determined to be approximately 1 : 1 by inductively coupled plasma (ICP) analysis, which is in agreement with the crystallographic results. The valence states of the metal ions were confirmed by bond-valence-sum (BVS) calculations and X-ray photoelectron spectroscopy (XPS) (Table S5, Fig. S69–S90†).

Intriguingly, these compounds present a variety of colors (Fig. 4b), that are affected by several factors. For example, Fe-containing compounds are easily oxidized, and their colors can be changed from yellow to red when exposed to air (Fig. S91†). The colors of Co constructed frameworks are related to the framework density and chelated ligands. Doubly interpenetrated **AlOC-99** presents darker color when compared with non-interpenetrated **AlOC-112**. Furthermore, the colors of 4-FBA coordinated frameworks (*e.g.*, **AlOC-102**) are also different from that of BA modified structures due to the electron-withdrawing effects of F centers (*e.g.*, **AlOC-99**). Diffuse reflectance spectroscopy measurements were performed on all complexes to better understand their optical absorption properties (Fig. S92–S95†).

Catalytic performance

The aldol reaction is a basic transformation in creating new carbon–carbon bonds and β-hydroxyl carbonyl compounds.[59] Considering the higher stability and catalytically active sites (unsaturated transition metals) on the Al_4O_4 support, three representative AlOCs (**AlOC-99**, **AlOC-109** and **AlOC-112**) were used as catalysts for the direct aldol reaction of acetone and nitro-substituted aromatic aldehyde in DMSO. The catalytic results are summarized in Table S6.†

In the presence of 10 mmol% catalysts, all three AlOCs show high catalytic activities giving desired aldol products in 79–88% yield. Upon completion of the reaction, all of them could be readily recovered by centrifugation and reused for the next cycle without significant loss of activity. The yield after three consecutive runs of **AlOC-109** can still remain 88% for isolated products. PXRD exhibited that the recycled sample retained high crystallinity after catalysis (Fig. S96†). In order to explore the impact of penetration on performance, the amount of catalyst is reduced to 5 mmol%, and mesoporous frameworks afford higher yield (67% for **AlOC-109**, and 68% for **AlOC-112**) compared with doubly interpenetrated **AlOC-99** (48%). This suggests that the catalytic reactions with a low content catalyst are related to the specific surface area. Besides, the control experiment without catalyst loading was also performed, and no condensation product can be observed, indicating that these crystals possess catalytic capability.

The probable catalytic mechanism is shown in Fig. 5.[60] First, the Co centers with unsaturated coordination sites polarize the carbonyl group of acetone, leading to the dissociation of the α-proton and generating a metal enolate. The oxygen atoms on BAs bond to the α-proton and leave the Co center transitorily. Then, 4-nitrobenzaldehyde combined with the metal enolate through C–C coupling, and condensation products can be obtained.

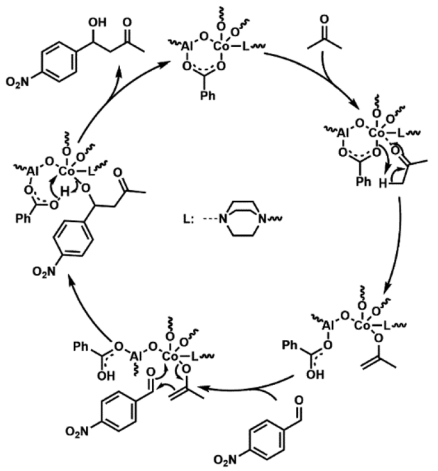

Fig. 5 Probable catalytic mechanism for the aldol condensation reaction by using AlOC-99, AlOC-109 and AlOC-112 as catalysts.

Conclusions

This is not only the first time that the γ-alumina moiety is found in crystalline porous compounds but it also serves as a support for loading various metal ions. The incorporation of hetero-metallic ions broadens the scope and potential applications of framework materials. This work provides a typical catalytic molecular model and demonstrates the unambiguous connections between the support (γ-alumina moiety) and catalytically active metal ions at the atomic level. Such γ-alumina moiety-supported materials can provide a reference for the catalytic system to achieve the hetero-disperse requirement meanwhile exposing as many catalytic sites as possible.

Data availability

All data supporting this study are available from article and ESI.† The raw data files are available from author upon reasonable request.

Author contributions

All authors contributed extensively to the work presented in this paper. J. Zhang and W.-H. Fang conceived the research project. Y.-J. Liu performed the synthesis and characterization experiments. Y. Yu performed catalytic experiments. Y.-F. Sun assisted in the data collection. W.-H. Fang and Y.-J. Liu wrote the manuscript and the ESI with input from the other authors.

Conflicts of interest

There are no conflicts to declare.

Acknowledgements

This work was supported by the National Key Research & Development Program of China (2021YFA1501500), National Natural Science Foundation of China (92061104, 21935010 and 21973096), Natural Science Foundation of Fujian Province (2021J06035) and Youth Innovation Promotion Association CAS (2021081).

Notes and references

1 P. Feng, X. Bu and G. D. Stucky, *Nature*, 1997, **388**, 735.
2 R. Banerjee, H. Furukawa, D. Britt, C. Knobler, M. O'Keeffe and O. M. Yaghi, *J. Am. Chem. Soc.*, 2009, **131**, 3875.
3 R. Simancas, D. Dari, N. Velamazán, M. T. Navarro, A. Cantín, J. L. Jordá, G. Sastre, A. Corma and F. Rey, *Science*, 2010, **330**, 1219.
4 Z. Wang, J. Yu and R. Xu, *Chem. Soc. Rev.*, 2012, **41**, 1729.
5 J. Cejka, A. Corma and S. Zones, *Zeolites and Catalysis. Synthesis, Reactions and Applications*, Wiley, Weinheim, 2010.
6 C. Sun, Z. Liu, S. Wang, H. Pang, R. Bai, Q. Wang, W. Chen, A. Zheng, W. Yan and J. Yu, *CCS Chem.*, 2021, **3**, 189.
7 S.-T. Zheng, T. Wu, F. Zuo, C. Chou, P. Feng and X. Bu, *J. Am. Chem. Soc.*, 2012, **134**, 1934.
8 E. E. Knyazeva and I. I. Ivanova, *Pet. Chem.*, 2019, **59**, 262.
9 X. Luo, Y. Cao, T. Wang, G. Li, J. Li, Y. Yang, Z. Xu, J. Zhang, Q. Huo, Y. Liu and M. Eddaoudi, *J. Am. Chem. Soc.*, 2016, **138**, 786.
10 H. Wang, L. Han, D. Zheng, M. Yang, Y. H. Andaloussi, P. Cheng, Z. Zhang, S. Ma, M. J. Zaworotko, Y. Feng and Y. Chen, *Angew. Chem., Int. Ed.*, 2020, **59**, 6263.
11 K. Williams, L. Meng, S. Lee, L. Lux, W. Gao and S. Ma, *Inorg. Chem. Front.*, 2016, **3**, 393.
12 S.-Y. Zhang, Z.-Y. Wang, J. Gao, K. Wang, E. Gianolio, S. Aime, W. Shi, Z. Zhou, P. Cheng and M. J. Zaworotko, *Chem*, 2019, **5**, 1609.
13 X.-C. Huang, Y.-Y. Lin, J.-P. Zhang and X.-M. Chen, *Angew. Chem., Int. Ed.*, 2006, **45**, 1557.
14 F. Wang, Z.-S. Liu, H. Yang, Y.-X. Tan and J. Zhang, *Angew. Chem., Int. Ed.*, 2011, **50**, 450.
15 K. S. Park, Z. Ni, A. P. Côté, J. Y. Choi, R. Huang, F. J. Uribe-Romo, H. K. Chae, M. O'Keeffe and O. M. Yaghi, *Proc. Natl. Acad. Sci. U.S.A.*, 2006, **103**, 10186.
16 N. T. T. Nguyen, H. Furukawa, F. Gándara, H. T. Nguyen, K. E. Cordova and O. M. Yaghi, *Angew. Chem., Int. Ed.*, 2014, **53**, 10645.
17 J. Zhang, T. Wu, C. Zhou, S. M. Chen, P. Y. Feng and X. H. Bu, *Angew. Chem., Int. Ed.*, 2009, **48**, 2542.
18 H.-X. Zhang, F. Wang, H. Yang, Y.-X. Tan, J. Zhang and X. Bu, *J. Am. Chem. Soc.*, 2011, **133**, 11884.
19 Y. Kang, F. Wang, J. Zhang and X. Bu, *J. Am. Chem. Soc.*, 2012, **134**, 17881.
20 H. Li, A. Laine, M. O'Keeffe and O. M. Yaghi, *Science*, 1999, **283**, 1145.
21 P. Feng, X. Bu and N. Zheng, *Acc. Chem. Res.*, 2005, **38**, 293.
22 J. Zhang, X. Bu, P. Feng and T. Wu, *Acc. Chem. Res.*, 2020, **53**, 2261.
23 N. F. Zheng, X. H. Bu and P. Y. Feng, *Nature*, 2003, **426**, 428.
24 K. S. Lokare, N. Frank, B. Braun-Cula, I. Goikoetxea, J. Sauer and C. Limberg, *Angew. Chem., Int. Ed.*, 2016, **55**, 12325.
25 B. Nohra, H. El Moll, L. M. Rodriguez Albelo, P. Mialane, J. Marrot, C. Mellot-Draznieks, M. O'Keeffe, R. N. Biboum, J. Lemaire, B. Keita, L. Nadjo and A. Dolbecq, *J. Am. Chem. Soc.*, 2011, **133**, 13363.
26 L. M. Rodriguez-Albelo, A. R. Ruiz-Salvador, A. Sampieri, D. W. Lewis, A. Gómez, B. Nohra, P. Mialane, J. Marrot, F. Sécheresse, C. Mellot-Draznieks, R. Ngo Biboum, B. Keita, L. Nadjo and A. Dolbecq, *J. Am. Chem. Soc.*, 2009, **131**, 16078.
27 G. Verma, S. Butikofer, S. Kumar and S. Ma, *Top. Curr. Chem.*, 2020, **378**, 4.
28 B. Hou, C. Qin, C. Sun, X. Wang and Z. Su, *CCS Chem.*, 2021, **3**, 287.
29 L.-D. Lin, D. Zhao, X.-X. Li and S.-T. Zheng, *Chem.–Eur. J.*, 2019, **25**, 442.
30 D. Braga, L. Maini, P. P. Mazzeo and B. Ventura, *Chem.–Eur. J.*, 2010, **16**, 1553.
31 L. Chong, H. G. Mao, Y. Q. Sun and J. L. Song, *Inorg. Chem.*, 2004, **43**, 1964.
32 J. P. Lang, Q. F. Xu, R. X. Yuan and B. F. Abrahams, *Angew. Chem., Int. Ed.*, 2004, **43**, 4741.
33 L.-D. Lin, C.-C. Deng, D. Zhao, X.-X. Li and S.-T. Zheng, *Chem.–Eur. J.*, 2018, **24**, 251.
34 Y. Xie, D. Kocaefe, Y. Kocaefe, J. Cheng and W. Liu, *Nanoscale Res. Lett.*, 2016, **11**, 259.
35 R. G. Pearson, *J. Am. Chem. Soc.*, 1963, **85**, 3533.
36 G. Paglia, C. E. Buckley, A. L. Rohl, B. A. Hunter, R. D. Hart, J. V. Hanna and L. T. Byrne, *Phys. Rev. B*, 2003, **68**, 144110.
37 B. C. Lippens and J. H. De Boer, *Acta Crystallogr.*, 1964, **17**, 1312.
38 W. W. Wendlandt and H. G. Hecht, *Reflectance Spectroscopy*, Interscience, New York, 1966.
39 G. M. Sheldrick, *SHELXL-2014 Program for Crystal Structure Solution and Refinement*, Univerity of Göttingen, Göttingen, Germany, 2014.
40 G. D. Piero, M. Cesari, G. Dozzi and A. Mazzei, *J. Organomet. Chem.*, 1977, **129**, 281.
41 C. Schnitter, A. Klemp, H. W. Roesky, H.-G. Schmidt, C. Röpken, R. Herbst-Irmer and M. Noltemeyer, *Eur. J. Inorg. Chem.*, 1998, 2033.
42 C. Jeff Harlan, E. G. Gillan, S. G. Bott and A. R. Barron, *Organometallics*, 1996, **15**, 5479.
43 A. C. Stelzer, P. Hrobárik, T. Braun, M. Kaupp and B. Braun-Cula, *Inorg. Chem.*, 2016, **55**, 4915.
44 S. Abeysinghe, K. W. Corum, D. L. Neff, S. E. Mason and T. Z. Forbes, *Langmuir*, 2013, **29**, 14124.
45 S. Abeysinghe, D. K. Unruh and T. Z. Forbes, *Inorg. Chem.*, 2013, **52**, 5991.
46 K. W. Corum, M. Fairley, D. K. Unruh, M. K. Payne, T. Z. Forbes and S. E. Mason, *Inorg. Chem.*, 2015, **54**, 8367.
47 C. M. Hong, R. G. Bergman, K. N. Raymond and F. D. Toste, *Acc. Chem. Res.*, 2018, **51**, 2447.
48 D. Zhang, T. K. Ronson, S. Güryel, J. D. Thoburn, D. J. Wales and J. R. Nitschke, *J. Am. Chem. Soc.*, 2019, **141**, 14534.
49 Y.-P. He, L.-B. Yuan, G.-H. Chen, Q.-P. Lin, F. Wang, L. Zhang and J. Zhang, *J. Am. Chem. Soc.*, 2017, **139**, 16845.
50 T. Yamada and H. Kitagawa, *J. Am. Chem. Soc.*, 2009, **131**, 6312.
51 J. Zhang, L. Wojtas, R. W. Larsen, M. Eddaoudi and M. J. Zaworotko, *J. Am. Chem. Soc.*, 2009, **131**, 17040.

52 Q. Lin, X. Bu, C. Mao, X. Zhao, K. Sasan and P. Feng, *J. Am. Chem. Soc.*, 2015, **137**, 6184.
53 A. L. Spek, *J. Appl. Crystallogr.*, 2003, **36**, 7.
54 M. Kruk and M. Jaroniec, *Chem. Mater.*, 2001, **13**, 3169.
55 S. Yang, X. Song, P. Zhang and L. Gao, *ACS Appl. Mater. Interfaces*, 2015, **7**, 75.
56 X. Fan, F. Yuan, D. Li, S. Chen, Z. Cheng, Z. Zhang, S. Xiang, S.-Q. Zang, J. Zhang and L. Zhang, *Angew. Chem., Int. Ed.*, 2021, **60**, 12949.
57 H. Wang, J. Getzschmann, I. Senkovska and S. Kaskel, *Microporous Mesoporous Mater.*, 2008, **116**, 653.
58 M. Andrzejewski and A. Katrusiak, *J. Phys. Chem. Lett.*, 2017, **8**, 279.
59 X. Yang, P. K. Majhi, H. Chai, B. Liu, J. Sun, T. Liu, Y. Liu, L. Zhou, J. Xu, J. Liu, D. Wang, Y. Zhao, Z. Jin and Y. R. Chi, *Angew. Chem., Int. Ed.*, 2021, **60**, 159.
60 S. Rojas-Buzo, P. García-García and A. Corma, *Green Chem.*, 2018, **20**, 3081.